Water Resources Research

RESEARCH ARTICLE
10.1029/2024WR037139

Global Flood Projection and Socioeconomic Implications Under a Deep Learning Framework

Shengyu Kang[1], **Jiabo Yin**[1], **Louise Slater**[2], **Pan Liu**[1], **Fubao Sun**[3], **Dedi Liu**[1], and **Jun Xia**[1]

[1]State Key Laboratory of Water Resources Engineering and Management, Wuhan University, Wuhan, PR. China, [2]School of Geography and the Environment, University of Oxford, Oxford, UK, [3]Xinjiang Key Laboratory of Water Cycle and Utilization in Arid Zone, Xinjiang Institute of Ecology and Geography, Chinese Academy of Sciences, Urumqi, China

Special Collection:
Advancing Interpretable AI/ML Methods for Deeper Insights and Mechanistic Understanding in Earth Sciences: Beyond Predictive Capabilities

Key Points:

- We improve the performance of streamflow simulation by developing a physics-constrained deep learning framework
- We project future changes in the bivariate river flood peak and volume in 8,583 catchments based on a cascade model chain
- The world is projected to experience doubled flood risk by the late 21st century, affecting trillions of USD and billions of people

Supporting Information:

Supporting Information may be found in the online version of this article.

Correspondence to:
J. Yin,
jboyn@whu.edu.cn

Citation:
Kang, S., Yin, J., Slater, L., Liu, P., Sun, F., Liu, D., & Xia, J. (2025). Global flood projection and socioeconomic implications under a deep learning framework. *Water Resources Research*, *61*, e2024WR037139. https://doi.org/10.1029/2024WR037139

Received 15 JAN 2024
Accepted 8 MAY 2025

Author Contributions:
Conceptualization: Jiabo Yin
Investigation: Pan Liu
Methodology: Shengyu Kang, Louise Slater, Fubao Sun
Supervision: Louise Slater
Writing – original draft: Shengyu Kang, Jiabo Yin
Writing – review & editing: Jiabo Yin, Pan Liu, Fubao Sun, Dedi Liu

Abstract As the planet warms, the frequency and severity of weather-related hazards such as floods are intensifying, posing substantial threats to communities around the globe. Rising flood peaks and volumes claim lives, damage infrastructure, and compromise access to essential services. However, the physical mechanisms behind global flood evolution are still uncertain, and their implications for socioeconomic systems remain unclear. In this study, we leverage a supervised machine learning technique to identify the dominant factors influencing daily streamflow. We then develop a physics-constrained cascade model chain which assimilates water and heat transport processes to project the bivariate risk of flood peak and volume, along with its socioeconomic consequences. To achieve this, we develop a hybrid deep-learning-hydrological model with bias-corrected outputs from 20 global climate models from CMIP6 under four shared socioeconomic pathways. Our results project considerable increases in flood risk under the medium to high-end emission scenario (SSP3-7.0) over most catchments of the globe. The median future joint return period decreases from 50 years to around 27.6 years, with 186 trillion USD and 4 billion people exposed. Downwelling shortwave radiation is identified as the dominant factor driving changes in daily streamflow, accelerating both terrestrial evapotranspiration and snowmelt. As future scenarios project enhanced global warming along with an increase in precipitation extremes, a heightened risk of widespread flooding is foreseen. This study aims to provide valuable insights for policymakers developing proactive strategies to mitigate the risks associated with river flooding under climate change.

Plain Language Summary Climate change is causing more weather-related hazards like storms and floods, which are dangerous for communities around the globe. However, changes in the peak and volume of floods and their potential drivers under a warming climate are not well understood, which complicates the projection of their socioeconomic implications. Our results indicate that if medium to high-end emissions continue until the end of the 21st century, an increase in flood risk could affect assets worth an estimated 186 trillion USD and potentially impact about 4 billion people. By the end of the 21st century, increased global warming coupled with intensified precipitation extremes are projected to become the dominant drivers of streamflow, resulting in more frequent and increasingly perilous floods. Our findings provide useful information to policymakers designing plans to address the intensification of flood risk across the globe.

1. Introduction

Global warming has raised the atmospheric water vapor holding capacity, altering the energy budget and water cycle (Allan et al., 2020). Changes in temperature affect global climate patterns, leading to shifts in hydrological variables such as precipitation and evapotranspiration, thus complicating the spatiotemporal distribution of hydrological extremes (Ostad-Ali-Askari et al., 2020; Samset et al., 2019). Some regions may experience more intense and prolonged droughts, while others have witnessed increasing risks of rainstorms and river floods (Donat et al., 2016; F. Zhang et al., 2021). Consequently, numerous studies have expressed concerns regarding the elevated risk of flooding and its negative impacts on ecosystems, economy, and society (Hoq et al., 2021; Mohanty et al., 2020). However, the physical mechanisms behind flood evolution are diverse and complex, manifesting differently across various climates and geographical regions (Berghuijs et al., 2019; Mao et al., 2019). The extent of damage and the socioeconomic implications of floods, therefore, vary significantly across different geographical regions, land use/land cover (LULC) types, and the resilience of the affected communities. Understanding these mechanisms is crucial for designing effective strategies to mitigate the diverse challenges posed by floods.

Flood simulation and projection are essential for understanding flood dynamics, but both have large uncertainties stemming from limitations in hydrological modeling (HM) (Nearing et al., 2024). Particularly, changes in LULC and human water management can alter natural hydrological processes, challenging conventional hydrological simulation by physical models (Gangrade et al., 2018). Global climate models (GCMs) provide a comprehensive prognosis of Earth's future climate by modeling complex interactions among atmospheric, oceanic, land, and ice components, which help project changes including extreme weather events like floods. Recently, machine learning (ML) and deep learning (DL) methodologies have been increasingly integrated into HM, offering innovative approaches to enhance the accuracy of streamflow simulation and projection by assimilating big data from various sources (Nearing et al., 2021; S. Yang et al., 2020). Among ML/DL models, the Long Short-Term Memory (LSTM) model, in particular, has promising performance and offers valuable insights into parameterizing non-linear hydrological processes. For example, Liu et al. (2021) used ML to enhance the simulation of a Global Hydrological Model (GHM) at 2,062 gauging stations globally. More recently, Kang et al. (2023) introduced a hybrid HM-LSTM model designed to project future flood risks in China. However, additional modifications are required to improve global-scale hybrid hydrological models, as improper variable inputs may introduce noise, and flood generation mechanisms are likely to differ across climatic subdivisions.

Besides the challenges of flood simulation and projection, the question of how to quantify flood risks under climate change is also a hot issue. Floods are natural phenomena which can be described by multiple characteristics including the peak flow, flood waveform, volume, or duration (Brunner, 2023). However, many studies only assess a singular flood characteristic, which may lead to an incomplete picture of flood dynamics (Maurer et al., 2018; Q. Zhou et al., 2021). For instance, floods with large volumes or high backward peaks—where the highest flow occurs later in the event—can pose substantial challenges for reservoir management and infrastructure resilience. Therefore, the interdependence of different features should be considered in flood risk assessment. Many studies have explored the complex nature of flooding in a changing climate, using copula-based approaches in particular for describing marginal distributions. For example, Hu et al. (2022) examined the consequences of climate change on flood magnitudes in the Yangtze River using a bivariate approach, and estimated the flood peak and volume quantiles by incorporating a most likely realization method. To our knowledge, there is a notable absence of studies that project the future risk of river bivariate flood peak and volume at a global scale, and even fewer works have achieved a robust flood projection by employing a physics-based ML/DL framework.

While hydrologists have focused intensely on the physical processes within climate and hydrological model simulations, the equally critical aspects of exposure and vulnerability have not received comparable attention. This discrepancy raises concerns that our understanding of the socioeconomic implications of floods is less developed than the numerical models used to calculate the flood magnitude or frequency themselves (Smith et al., 2019). Floods impact socioeconomic systems by damaging infrastructure, disrupting businesses, causing public health issues, displacing communities, straining financial services, and harming the environment (Botzen et al., 2009; Vousdoukas et al., 2018). Climate change intensifies weather patterns and increases heavy rainfall frequency, exacerbating river flooding and amplifying socio-economic challenges (Tellman et al., 2021). In early 2023, California's infrastructure suffered significant damage due to flooding, including the destruction of roads and bridges, while numerous homes were inundated, displacing residents and leading to a critical reassessment of flood management strategies (Schubert et al., 2024). The expected rise in both flood frequency and severity in a warming Earth as a consequence of global climate change poses a substantial risk for future socio-ecosystems, with potentially severe humanitarian and economic impacts and long-term negative effects on economic growth (Hirabayashi et al., 2021). To assess the future socioeconomic landscape, the International Institute for the Organization for Economic Co-operation and Development (OECD, Dellink et al., 2017) and Applied Systems Analysis (IIASA, Kc & Lutz, 2017) released global estimates of future GDP and population. However, few studies have assessed the socioeconomic implications of future flooding at the global scale with a bivariate framework.

Here, we aim to explore the physical mechanisms behind bivariate flood evolution and their implications for the socioeconomic system at a global scale, which utilizes twenty bias-corrected GCMs under 4 shared socioeconomic pathways (SSPs) (i.e., SSP1-2.6, SSP2-4.5, SSP3-7.0, and SSP5-8.5), a DL model and 5 HMs. To furnish valuable information for streamflow simulations, we first employ a supervised ML model to identify dominant meteorological factors in driving changes in streamflow. Then, we project future daily streamflow in 8,583 global catchments by combining climate model and our developed physics-constrained DL framework. Subsequently, the joint distributions of flood peak and 7-day flood volume are established by using a set of copula functions during both historical (1985–2014) and future (2071–2100) periods. The changes in bivariate flood characteristics are then assessed by utilizing the most realization method, and the socioeconomic implications to elevated flood risks are quantified. The overall workflow of our study is summarized in Figure 1. Finally, we attempt to explain the physical mechanisms of flood risk shifts under climate change.

2. Material and Data

2.1. Global In Situ Observation Data

We gather daily streamflow records at the outlets of 22,538 catchments globally from 1950 to 2021, using a mix of worldwide and national streamflow databases as follows: (a) Brazilian streamflow data from the Brazilian National Water Agency (ANA Hidroweb), (b) Canadian streamflow data from the Water Survey of Canada, (c) Chinese streamflow data from the Hydroinformatic Data Centre and 9 water resources commissions affiliated to the Ministry of Water Resources of China, (d) Mexican streamflow data from the Comisión Nacional del Agua (CONAGUA), (e) UK streamflow data from the National River Flow Archive, (f) US streamflow data from the US Geological Survey (USGS), and (g) global streamflow data set from the Global Runoff Data Centre. To ensure data quality, we implement a three-stage check: initially, stations with changes in measurement instruments or station datums are removed to maintain data consistency. Then, we filter out 12,940 stations that failed to provide a minimum of 20 years of valid data, with each year having less than 10% of incomplete data. Finally, catchments with poor hydrological simulation performance, indicated by a Kling-Gupta efficiency (KGE) value below 0.5 in all models, are excluded. These rigorous steps resulted in 8,583 catchments that are representative of a broad spectrum of global climate regimes.

2.2. ERA5-Land and Aridity Index Data Set

The ERA5-Land data represents an upgraded global data set specifically designed for the land segment in the ERA5 (Muñoz-Sabater et al., 2021). Developed by the European Centre for Medium-Range Weather Forecasts (ECMWF), ERA5-Land offers detailed and comprehensive information on various parameters, including temperature, lakes, snow, soil water, etc. Encompassing the entire planet and boasting a resolution of approximately 9 km, ERA5-Land spans a considerable temporal range, providing hourly data from 1950 to the present. This data set is distinguished by its improved accuracy, spatial resolution, and temporal consistency, making it a popular asset for a wide range of applications, including climate dynamics, HM, and the assessment of environmental changes (Han et al., 2024). In this study, we utilize hourly series of six primary variables: 2 m air temperature (T_{2m}), 2 m dew point temperature (T_{dew}), air pressure (ps), precipitation (pr), 10 m wind speed (wind), surface downwelling longwave radiation (rlds), and surface downwelling shortwave radiation (rsds, also known as global solar radiation). For instantaneous variables defined in ERA5-Land, we use Climate Data Operators (CDO) for daily averaging. For the accumulated variables, we use the value of the last time step of each integration interval, which is the daily accumulated flux.

To understand global flood dynamics across various climatic regions, we additionally use the aridity index (AI) from the Global AI and Potential Evapotranspiration Database-Version 3, offering high-resolution global data spanning the period from 1970 to 2000 (Zomer et al., 2022). The data set focus on evapotranspiration processes and precipitation deficit concerning potential vegetative growth, employing the FAO-56 Penman-Monteith Reference Evapotranspiration (ET_0) equation. The AI, a key metric, reflects the ratio between precipitation and ET_0, reflecting the balance between rainfall and vegetation water demand on an annual basis. It has gained extensive use for assessing precipitation availability in relation to water demand and for partitioning climate zones, which has been widely employed in hydrological research (e.g., Fang et al., 2024).

2.3. Bias-Corrected Climate Model Outputs and Socioeconomic Data

Originally released in 2015, the inaugural version of the NASA Earth Exchange Global Daily Downscaled Projections (NEX-GDDP) archive aimed to improve public awareness and support the scientific community in understanding climate change impacts on a finer scale (Thrasher et al., 2022). Currently, the latest version of

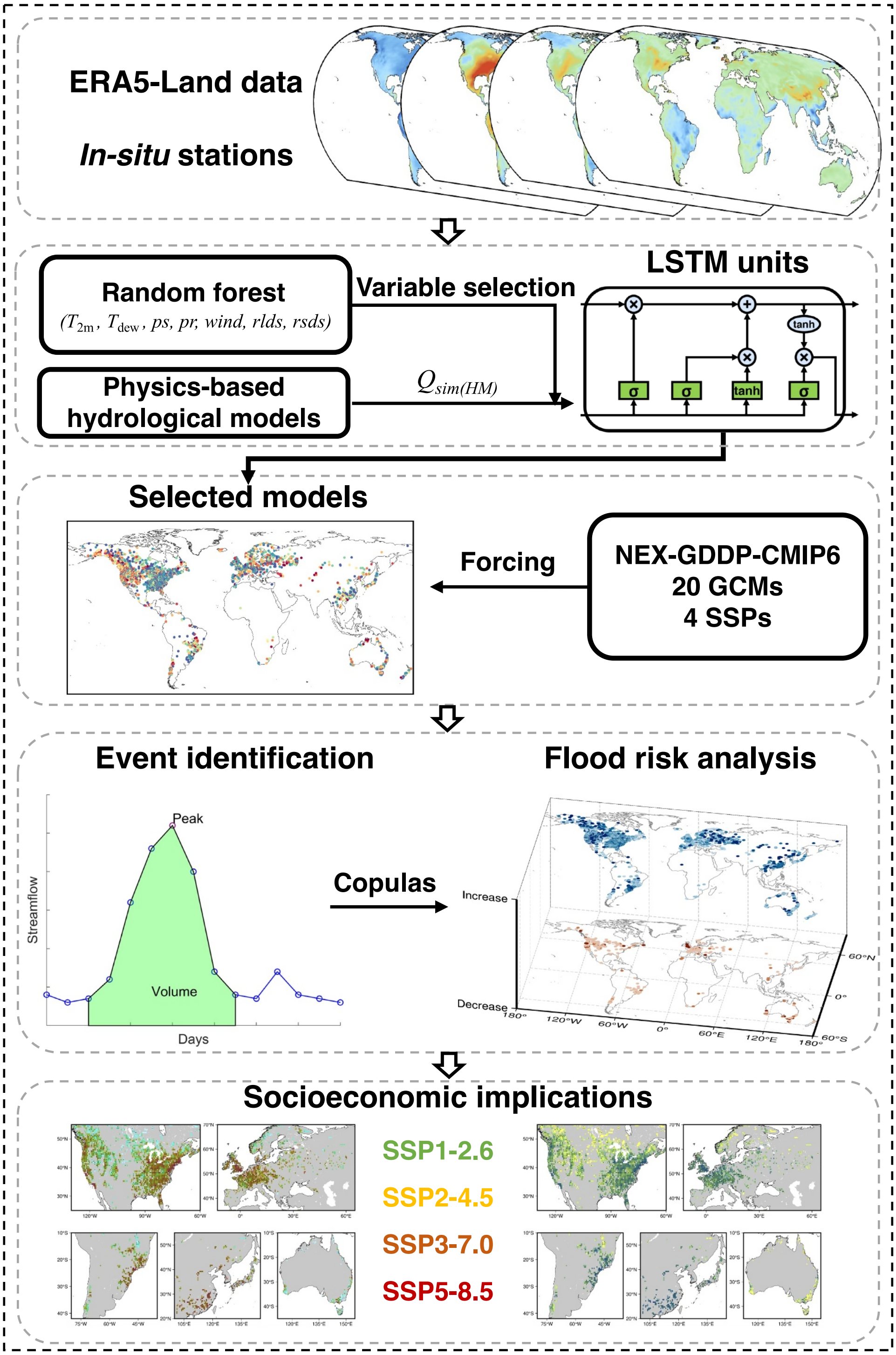

Figure 1. Flowchart of deep learning-based flood projection and socioeconomic impact assessment.

NEX-GDDP is provided for five CMIP6 experiments (historical, SSP1-2.6, SSP2-4.5, SSP3-7.0, and SSP5-8.5) at https://www.nccs.nasa.gov/services/data-collections/land-based-products/nex-gddp-cmip6. The NEX-GDDP-CMIP6 archive offers a global collection of bias-adjusted, high-resolution (0.25° × 0.25°), and continuous daily climate projections over land (Park et al., 2023). To assess climate model uncertainty, a large set of multi-model ensembles comprising 20 GCMs is employed (See Table S1 in Supporting Information S1). The considered climate variables are daily minimum temperature ($T_{\min}$), daily mean temperature (T_{mean}), daily maximum temperature ($T_{\max}$), wind speed (wind), surface downwelling longwave radiation (rlds), surface downwelling shortwave radiation (rsds), specific humidity (huss), relative humidity (hurs), and precipitation (pr).

To evaluate the socioeconomic implications of floods, we utilize population and GDP data under the four scenarios (i.e., SSP1-2.6, SSP2-4.5, SSP3-7.0, and SSP5-8.5) from IIASA and OECD to encompass diverse representations of climate change and adaptation. This data set employs a detailed demographic modeling approach, projecting national population and GDP by age, sex, and educational levels under different assumptions aligned with the SSP scenarios, accounting for future changes in fertility, mortality, migration, and education. Numerous studies have been carried out using this data set (O'Neill et al., 2020; Tang et al., 2022). However, the aforementioned data set relies on information that deviates slightly from data produced by the Chinese government, and does not incorporate adjustments under China's practical population policy (T. Jiang et al., 2018). Therefore, we utilize future GDP and population over China produced by T. Jiang et al. (2020), which are projected by localization parameters based on statistical yearbooks and population policy changes. These data sets have been extensively used to assess the socioeconomic implications of severe hydrologic events (e.g., Dai et al., 2022; Gu et al., 2020; Yin et al., 2022).

3. Methods

3.1. Calculation of Water Vapor-Related Parameters

Water vapor is a fundamental element within the hydrological cycle and holds a significant role in triggering precipitation extremes and flood hazards (Bengtsson, 2010). To determine water vapor parameters (i.e., huss and hurs), we use $T_{2\mathrm{m}}$ and T_{dew}, ensuring consistency with GCMs and compensating for discrepancies with ERA5-Land data. Specifically, based on the Clausius-Clapeyron relationship, we can first derive the saturation water vapor pressure via dry-bulb temperature (T):

$$e_{\mathrm{sat}}(T) = e_{\mathrm{s0}} \exp\left[\frac{L_v}{R_v}\left(\frac{1}{T_0} - \frac{1}{T}\right)\right] \tag{1}$$

where $T_0 = 273.16$ K and $e_{\mathrm{s0}} = 611$ Pa are the triple point of water and the reference saturated vapor pressure, respectively; R_v and L_v represent the gas constant for water vapor (461 J kg^{-1} K^{-1}) and the latent heat of vaporization (2.5×10^6 J kg^{-1}), respectively.

T_{dew} represents the temperature at which air reaches saturation while keeping the water vapor content and pressure constant. By incorporating values of $T_{2\mathrm{m}}$ and T_{dew} into Equation 1, we can effectively calculate the near-ground relative humidity:

$$\mathrm{hurs} = \frac{e_{\mathrm{sat}}(T_{\mathrm{dew}})}{e_{\mathrm{sat}}(T_{2\mathrm{m}})} \tag{2}$$

Specific humidity is defined as the proportion of water vapor mass to the entire mass of an air parcel, and it can be calculated using ps and T_{dew} data from ERA5-Land as follows (Simmons et al., 1999):

$$\mathrm{huss} = 0.622 \frac{e_{\mathrm{sat}}(T_{\mathrm{dew}})}{\mathrm{ps} - 0.378 e_{\mathrm{sat}}(T_{\mathrm{dew}})} \tag{3}$$

3.2. Identification of Dominant Streamflow Drivers and Hydrological Simulation

3.2.1. Supervised Machine Learning for Identifying Dominant Streamflow Drivers

The field of hydrology has evolved to a point where it now benefits from a considerable amount of data from diverse sources (Klingler et al., 2021). While this vast repository of information offers an immense addition of data to HMs, it can inadvertently introduce noise, thereby obscuring key insights in model performance. To elucidate the physical mechanisms driving changes in the hydrological cycle, we utilize a supervised ML technique, specifically random forest (RF), which proves efficient in ranking the importance of various variables contributing to a complex system (Gregorutti et al., 2017). Previous studies have quantified the sensitivity of meteorological factors to runoff using RF models (e.g., Kang et al., 2023), but it remains unclear whether these factors could enhance simulated streamflow or not. In particular, Breiman (2001) introduced the idea based on observing the effects of randomly shuffling each variable's values and measuring the impact on model accuracy. The importance of the jth variable can be defined as:

$$\mathrm{VI}(x^{v}) = \frac{1}{|\mathrm{TREE}_{v}|} \sum_{i \in \mathrm{TREE}_{v}} \frac{\sum_{j \in \mathrm{OOB}_{i}} \left(y_{j} - \hat{f}_{i}(x_{j}^{v})\right)^{2} - \sum_{j \in \mathrm{OOB}_{i}} \left(y_{j} - \hat{f}_{i}(x_{j}^{v*})\right)^{2}}{|\mathrm{OOB}_{i}|} \tag{4}$$

where VI represents the importance of variables, and TREE_v is the subset of all trees that selects the vth variable as predictor; OOB_i signifies the out-of-bag sample set of the ith tree, and y denotes observed streamflow; x^v and x^{v*} are the original and altered input data with the vth variable permuted, respectively; $\hat{f}_i$ symbolizes the model fitted by the ith tree. The equation measures the importance of each predictor variable by calculating the decrease in model accuracy when their values are randomly shuffled. This is assessed using the average change in error rates from out-of-bag samples across all trees in the forest, highlighting key variables influencing streamflow variations.

3.2.2. Estimation of Time Delay in Catchment Response

In HM, larger catchments typically show a longer response time to meteorological variables (Frisbee et al., 2012), as evidenced by the duration required for rainfall to traverse the catchment area to the outlet. Including the time delay within the physics-constrained ML/DL model enhances the model's ability to learn from the data, leading to an improved fit with the streamflow. In this study, we employ the following formula to quantify the relationship between time delay and catchment area (Ganguli & Merz, 2019):

$$D = 2.51 S^{0.4}[\mathrm{hours}] = 0.11 S^{0.4}[\mathrm{days}] \tag{5}$$

where D and S denote the time delay and the catchment area (km^2), respectively.

3.2.3. Physics-Constrained Deep Learning Modeling

Reliable hydrologic modeling is crucial for accurate prediction and effective management of water resources and environmental phenomena (Sahu et al., 2023). In this study, we introduce a new framework that integrates HMs with DL algorithms, which is a synthetic combination designed to enhance the accuracy of hydrological simulations (Kang et al., 2023). First, we employ five lumped HMs, namely the XAJ model (Zhao, 1992), the HBV model (Bergström & Forsman, 1973), the GR4J model (Perrin et al., 2003), the IHACRES model (Jakeman & Hornberger, 1993), and the SIMHYD model (Chiew et al., 2002), to serve as the basis for simulating the natural hydrological cycle. The parameter schemes for these models are detailed in Table S2 in Supporting Information S1. As human activities pose challenges to the simulation ability of HMs, particularly in heavily regulated basins, more sophisticated techniques are required to improve streamflow simulation by HMs (D. Jiang & Wang, 2019; Kang et al., 2023).

The LSTM network conceived by Hochreiter and Schmidhuber (1997), might address the above issue by assimilating noise in the data introduced by human activities. This capability is achieved through the mechanism of backpropagation through time, a process where the network learns from the temporal sequences of data, adjusting its internal parameters based on the error gradient of previous time steps. A typical LSTM unit comprises a cell, along with an input gate, an output gate, and a forget gate. These gates regulate the flow of information, allowing the network to effectively retain or discard data based on its relevance (Gers et al., 2000). The cell retains values across variable time intervals, and the input gate controls the incorporation of new information into the cell state. Concurrently, the forget gate decides which parts of the existing information to keep or discard, a critical function for managing the cell's memory. The output gate then selectively transfers information from the cell state to the next layer or time step. These operations are encapsulated as follows, which delineate a standard memory block within an LSTM structure:

$$i_t = \sigma(W_i \cdot [h_{t-1}; x_t] + b_i), \tag{6}$$

$$f_t = \sigma\left(W_f \cdot [h_{t-1}; x_t] + b_f\right), \tag{7}$$

$$o_t = \sigma(W_o \cdot [h_{t-1}; x_t] + b_o), \tag{8}$$

$$c_t = f_t \otimes c_{t-1} + i_t \otimes \tan h(W_c \cdot [h_{t-1}; x_t] + b_c), \tag{9}$$

$$h_t = o_t \otimes \tan h(c_t) \tag{10}$$

where x_t, i_t, o_t, and f_t represent the input variables, the input gate, the output gate, and the forget gate at time t, respectively. The terms c_t and h_t refer to the cell state and the hidden unit at the current time t, whereas c_{t-1} and h_{t-1} are their counterparts from the previous time step, $t - 1$. Initially, both the cell state and hidden state are initialized as zero arrays. The terms W_i, W_f, W_o, and W_c are the weight matrices; b_i, b_f, b_o, and b_c are the bias components; σ (·) and tan$h$ (·) are the sigmoid function and hyperbolic tangent function, both of which vary between 0 and 1. The model structure consists of a first LSTM layer with 128 units followed by a dropout layer for regularization, and a second LSTM layer with 64 units to further process the features. A fully connected layer is subsequently linked to the last LSTM layer, effectively transforming h_t into a new output.

To integrate physical principles into our DL framework, we employ a physics-constrained DL modeling that assimilates the output of the lumped hydrological models alongside high-importance water-heat variables. By explicitly feeding HM-derived streamflow simulations and key variables identified by RF into the LSTM, we guide the model to constrain fundamental hydrological processes and conservation laws. This approach ensures that the data-driven component does not diverge from established physical principles while learning from broader climate and catchment-specific patterns. In practice, we select water-heat variables ranking in the upper half of importance for each catchment (i.e., 5 out of 9), and then synchronize both these variables and the HM outputs to account for catchment-specific time delays. By calibrating the temporal alignment of these inputs, the LSTM usually better effectively captures the inherent lag in hydrological responses and streamflow generation. Consequently, this physics-constrained design enhances the interpretability and reliability of the hybrid model, ensuring the simulations remain consistent with physical laws and improve in both accuracy and climate relevance.

3.3. Bivariate Risk Assessment and Socioeconomic Implications

3.3.1. Copula-Based Bivariate Framework

Copulas offer a flexible and comprehensive tool for characterizing the interdependency within hydrological systems, making them widely employed in multivariate risk analysis (Li et al., 2022; B. Zhang et al., 2022). We employ a set of copula functions to establish a bivariate framework, linking the flood peak discharge (Q) and the 7-day flood volume (W). In this study, Q and W are defined in Figure S1 in Supporting Information S1 based on the annual maximum flood. Different countries recommend various distribution functions for flood analysis (Samuels et al., 2006); consequently, seven potential candidate distributions are used to approximate the marginal distributions of Q and W: Normal, Log-normal, Generalized extreme value, inverse Gaussian, Gamma, Weibull, and Pearson type-III. Additionally, the joint distributions are approximated by three candidate Archimedean copulas: Gumbel, Clayton and Frank. In the context of the joint return period (JRP), different forms such as "AND" (where the flood peak and volume both exceed the design value) and "OR" (where either the flood peak or the volume exceed the design value) represent various ways of interpreting the joint occurrence of events. For the floods considered in this study, the return period (RP) can be defined by considering the flood peak discharge and 7-day flood volume as follows (Brunner et al., 2016):

$$T_Q = \frac{M}{1 - P[Q \leq q]} = \frac{M}{1 - F_Q(q)} \tag{11}$$

$$T_W = \frac{M}{1 - P[W \leq w]} = \frac{M}{1 - F_W(w)} \tag{12}$$

where T_Q and T_W denote the RP of Q and W, respectively; M represents the average interval time between two successive flood events (equal to 1-year in this study); F_Q (F_W) is the probability cumulative function of Q (W); and P indicates the likelihood probability of occurrence.

Given that both high flood peaks and large flood volumes independently pose significant threats to infrastructure and the environment, we opt for the "OR" case in our JRP analysis:

$$T_{Q\cup W} = \frac{M}{P[Q \geq q \text{ or } W \geq w]} = \frac{1}{1 - C\big(F_Q(q),\ F_W(w)\big)} \tag{13}$$

where $T_{Q\cup W}$ represents the JRP of flood peak and volume and $C\,(\cdot)$ is the selected copula function.

It is worth noting that a single JRP can correspond to an infinite array of bivariate flood combinations, each with varying flood peaks and volumes; however, not every combination will occur in reality. To address this, we employ the most likely realization method, which selects the combinations of flood peak (q^*) and 7-day volume (w^*) with the highest probability of occurrence (Yin et al., 2023):

$$\left\{\begin{aligned} &(q^*, w^*) = \arg\max f(q,w) = c\big[F_Q(q),\ F_W(w)\big] f_Q(q) f_W(w) \\ &C\big(F_Q(q),\ F_W(w)\big) = 1 - \frac{M}{T_{Q\cup W}} \end{aligned}\right\} \tag{14}$$

where $f\,(q, w)$ denotes the joint probability density function of flood peak and volume; $f_Q\,(q)$ and $f_W\,(w)$ represent the probability density functions of Q and W; and $c\,(\cdot)$ symbolizes the probability density of the copula function. Owing to the intricacies and challenges in formulating analytical solutions for Equation 14, we resort to numerical methods to optimize its solution.

3.3.2. Quantifying Future Socioeconomic Implications of Flooding

To determine the socioeconomic implications of floods across diverse SSPs, we evaluate changes in flood occurrence within a bivariate context. First, we assess the socioeconomic implications for different geographic grid cells by combining the projected future population and GDP data with our flood simulation results from the multi-GCMs ensemble. Then, for grid cells spanning multiple catchments, we calculate their average values using the following formula:

$$E_i = \frac{1}{K} \sum_{k=1}^{K} \sum_{j \in CTA_i} \frac{T_{\text{his}}^j I\big(T_{\text{his}}^j - T_{\text{fur}}^j\big)}{T_{\text{fur}}^j |CTA_i|} \times A_i \tag{15}$$

where E denotes the socioeconomic implications; T_{his} and T_{fur} are the JRP during historical and future period; K is the total number of GCMs (20 in this study); $I\,(\cdot)$ is an indicator function (when $T_{\text{his}} - T_{\text{fur}} > 0$, $I = 1$; otherwise, $I = 0$); CTA$_i$ represents the set of catchments containing the ith grid cell; and A_i represents the asset, which is the GDP or population on the ith grid cell.

3.4. Robustness Analysis

While GCMs aim to emulate the physical processes within the climate system, their outputs are characterized by high uncertainty (Raju & Kumar, 2020). This uncertainty stems from inadequacies in representing the complexity of the climate system, uncertainties in downscaling methods, initial conditions, and challenges in greenhouse gas emission projections (Woldemeskel et al., 2014). Given the potential variations in sign and magnitude across different simulations, hypothesis testing is employed to assess the robustness of the computed outcomes (S. Zhou et al., 2022). Regarding changes in flood risk, the null hypothesis is that there is an equal probability of an increase in risk ($p = 0.5$). Assuming that the simulations of flood risk are independent, the probability of observing m out of n trials projecting an increased flood risk is represented by the following equation:

$$P = \frac{n!}{m!(n-m)!} p^m (1-p)^{n-m} \tag{16}$$

Based on the binomial distribution, a rejection of the null hypothesis is warranted if an increase in flood risk is observed in l of n flood simulations:

$$P_i(m \geq l) = \sum_{m=l}^{K|CTA_i|} \frac{(K|CTA_i|)!}{m!(K|CTA_i| - m)!} p^m \times (1-p)^{K|CTA_i|-m} < P_{\text{level}} \tag{17}$$

Where l stands for the minimum number of simulations needed to reject the null hypothesis and P_{level} denotes the probability corresponding to the chosen level of significance (set as 0.001 or 0.05 in this study).

4. Results

4.1. Dominant Streamflow Drivers and Hydrological Simulations

Prior to performing the hydrological simulations, we use supervised ML to discern the dominant factors of streamflow generation. By constructing an RF model with 300 trees and permuting the meteorological variables (i.e., T_{max}, T_{mean}, T_{min}, wind, hurs, huss, rlds, rsds, and pr), the dominant factors are identified for each catchment in Figure 2. Our findings reveal that downwelling shortwave radiation, as opposed to the more commonly emphasized rainfall-runoff processes in traditional hydrologic models, emerges as the most important factor influencing streamflow in various arid subregions (Figure 2c). The distinct predominance of downwelling shortwave radiation is notably pronounced in high-latitude areas like Scandinavia, and in mountainous regions including the Alps and the Rocky Mountains (Figure 2b), highlighting the substantial influence of topography. The spatial heterogeneity of the dominant factors also reveals the variations in mechanisms of streamflow generation across different regions. For instance, in the western Siberian Plain, where downwelling shortwave radiation also substantially influences streamflow, it is observed that the maximum flood events are more often produced by snow or mixed rain-snow conditions (S. Zhang et al., 2022). In the UK mainland and the US. West Coast, precipitation is usually the most important factor, probably due to flood evolution being predominantly driven by intense rainfall or excessive soil moisture in these regions. As the three factors most influencing catchment streamflow counts, we find that relative humidity, while being more uniformly distributed across latitudes, is not one of the most important factors in regions where the AI > 3 (Figures 2d–2f). This could be attributed to the fact that in arid regions, weak atmospheric moisture transport has a lesser impact on streamflow. Conversely, downwelling shortwave radiation and precipitation exert a weaker influence in the Southern Hemisphere, as snowmelt-dominated basins and mountainous regions are primarily situated in the Northern Hemisphere. Overall, while traditional lumped HMs often rely on precipitation feedback processes based on the unit hydrograph method, our RF model reveals that it is worth broadening this approach. We therefore employ the DL to reflect more complex hydrological processes, selectively using the top 50% of variables based on their importance in each catchment as inputs.

The distribution of KGE values under the physics-constrained DL framework is presented in Figure 3. In our comprehensive analysis encompassing a wide range of catchments, the GR4J and GR4J-LSTM models emerge as the most effective, achieving the highest KGE in 3,736 catchments. Following closely are the XAJ and XAJ-LSTM models, which demonstrate superior performance in 2,300 catchments. On the other hand, the IHACRES model, with its relatively simplistic assumptions, shows best performance in only 75 catchments; the IHACRES-LSTM achieves the highest simulation score in merely 327 catchments, marking IHACRES the least used among the 5 lumped HMs that incorporated DL adjustments. This suggests that the IHACRES model's oversimplified assumptions, such as the division between fast and slow streamflow, fall short in comparison to HMs based on soil layering assumptions (i.e., XAJ and GR4J). In the western Americas and Europe, the KGE is notably higher, benefiting from the extensive data available in these regions and the improved data extraction capabilities of DL (Figure 3b). This distribution reflects the varying suitability and effectiveness of these models in different hydrological contexts. Regarding the quality of the hydrological simulations, the XAJ-LSTM model stands out with its superior performance, achieving a median KGE of 0.764. This is closely followed by the GR4J-LSTM model, which also exhibits impressive results with a median KGE of 0.761. Notably, all the models enhanced with DL adjustment surpass their original lumped HM counterparts in terms of median KGE, underscoring the ability to complement water cycle processes by the integration of DL techniques (Figure 3c). Additionally, Table S3 in Supporting Information S1 presents the performance metrics for all evaluated models using various statistical measures. Integrating LSTM generally improves NSE and reduces MAE and RMSE

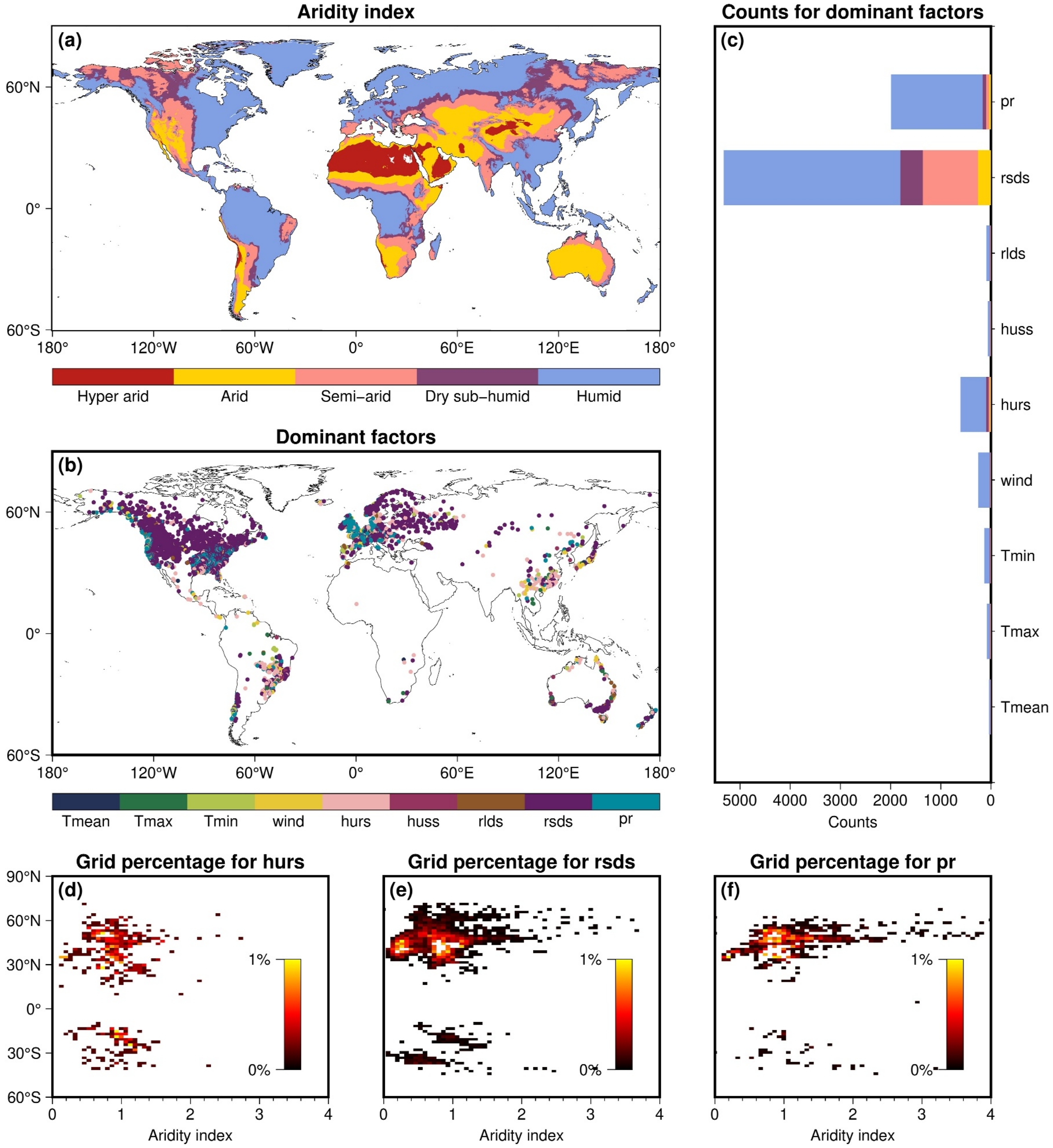

Figure 2. (a) Global aridity index and (b) identification of dominant factors in each catchment. (c) Statistics of the dominant factors in different aridity zones and the corresponding grid percentage of different aridity indices and latitudes for (d) *hurs*, (e) *rsds*, and (f) *pr*, respectively.

across most models. For example, the GR4J-LSTM model has an NSE of 0.497 compared to 0.468 for GR4J, and an MAE of 2.676 versus 2.808 for GR4J. Similarly, the XAJ-LSTM model achieves an NSE of 0.487 and an MAE of 2.714, compared to the base XAJ model's NSE of 0.422 and MAE of 2.981. Except for the XAJ-LSTM model's KGE, all other metrics show improvement with LSTM integration, indicating enhanced model performance. These results support the effectiveness of the physics-constrained DL framework across different hydrological models, underscoring the ability to complement water cycle processes by the integration of DL techniques. Overall, our physics-constrained DL framework enhances the simulation capacity for 39.1% (3,361 out of 8,583) of the catchments studied, thereby reducing uncertainty in our subsequent estimates of flood risks and socio-economic implications.

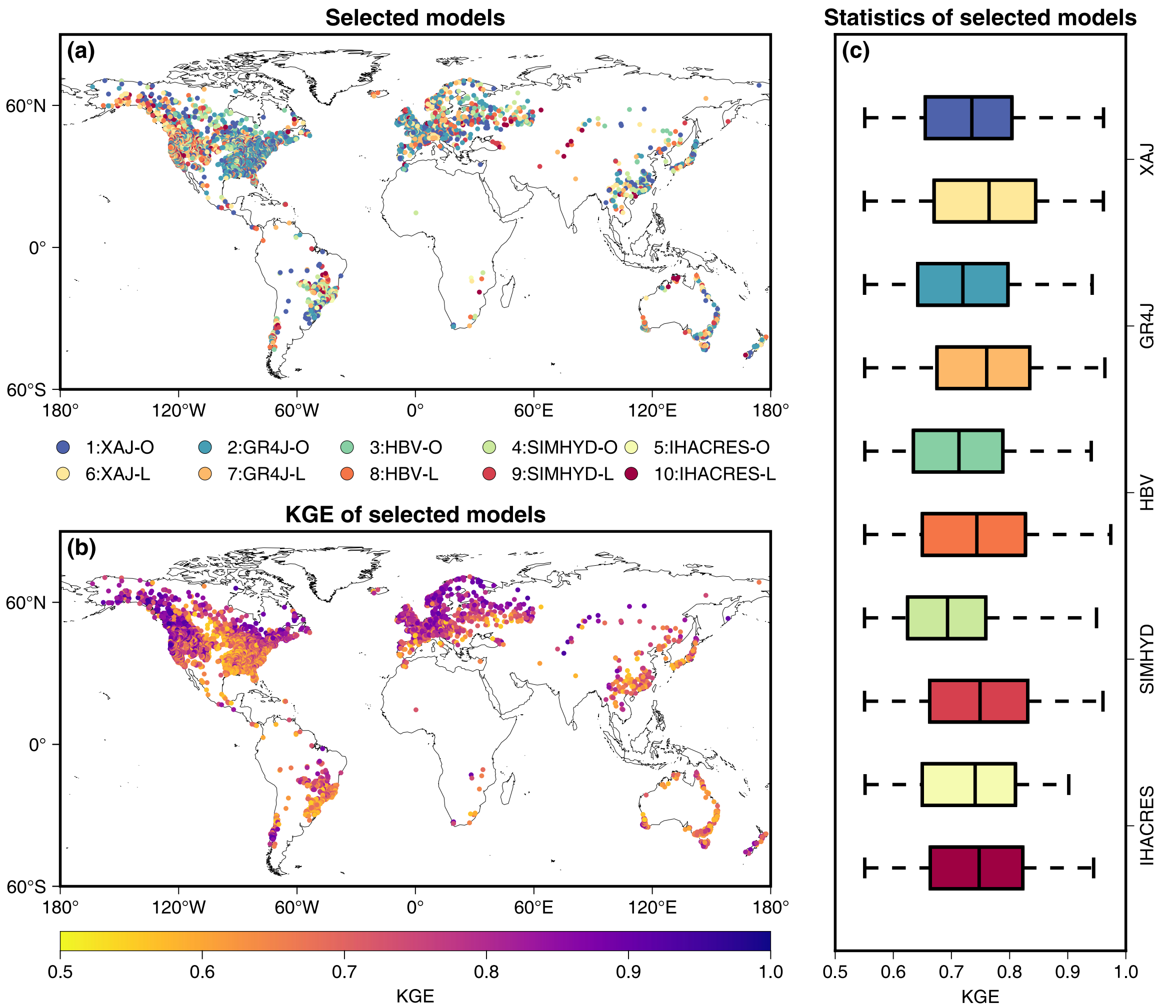

Figure 3. Results of global hydrological modeling (HM) under the physics-constrained deep learning-framework. (a) The best-performing (selected) HMs for each catchment and (b) their corresponding Kling-Gupta efficiency (KGE) values in the validation period. "−O" denotes the original lumped HM and "−L" denotes the HM after correction based on the Long Short-Term Memory network, respectively. (c) Statistical box plots of global KGE values in the validation period.

4.2. Projected Changes in Floods Under 50-Year Return Period

From the projected daily streamflow, obtained by applying the best-performing HMs with the twenty NEX-GDDP-CMIP6 climate models, we extract the annual maximum peak discharge and the 7-day maximum flood volume. The extracted values are then fitted to the various distributions outlined in Section 3.3.1. Each distribution is evaluated and determined by the minimum Bayesian Information Criterion method, ensuring an optimal balance between model fit and complexity. Figures 4 and 5 depict the relative changes in mean flood peaks and 7-day flood volumes under the 50-year historical RP projected by a multi-model ensemble composed of 20 GCMs. Our findings indicate that, even under the lowest level of carbon emissions (i.e., SSP1-2.6), substantial increases in flood peaks and volumes are projected in the catchments of the Colorado River Basin, the Missouri River Basin, the Volga River Basin, and the Yellow River Basin (Figures 4a and 5a). Specifically, under the SSP1-2.6 scenario, the median relative increase in flood volume across global catchments is projected to be 15.8%, while under SSP2-4.5, it rises to 17.7%. More pronounced increases are observed under SSP3-7.0 and SSP5-8.5 scenarios, with median relative increases of 21.3% and 23.8%, respectively (Figures 4e–4h). Similarly, for the 7-day flood volume in global catchments, the median relative increase under SSP1-2.6 is estimated at 14.1%, 15.4% for SSP2-4.5, 19.0% for SSP3-7.0, and 20.9% for SSP5-8.5 (Figures 5e–5h). These results underscore the escalating impacts of climate change on hydrological extremes across different future socioeconomic trajectories. It is noteworthy that, as carbon emissions escalate, the overall trend in the histograms does not simply shift toward more intense flooding uniformly. Instead, we observe that catchments experiencing smaller changes (lesser than

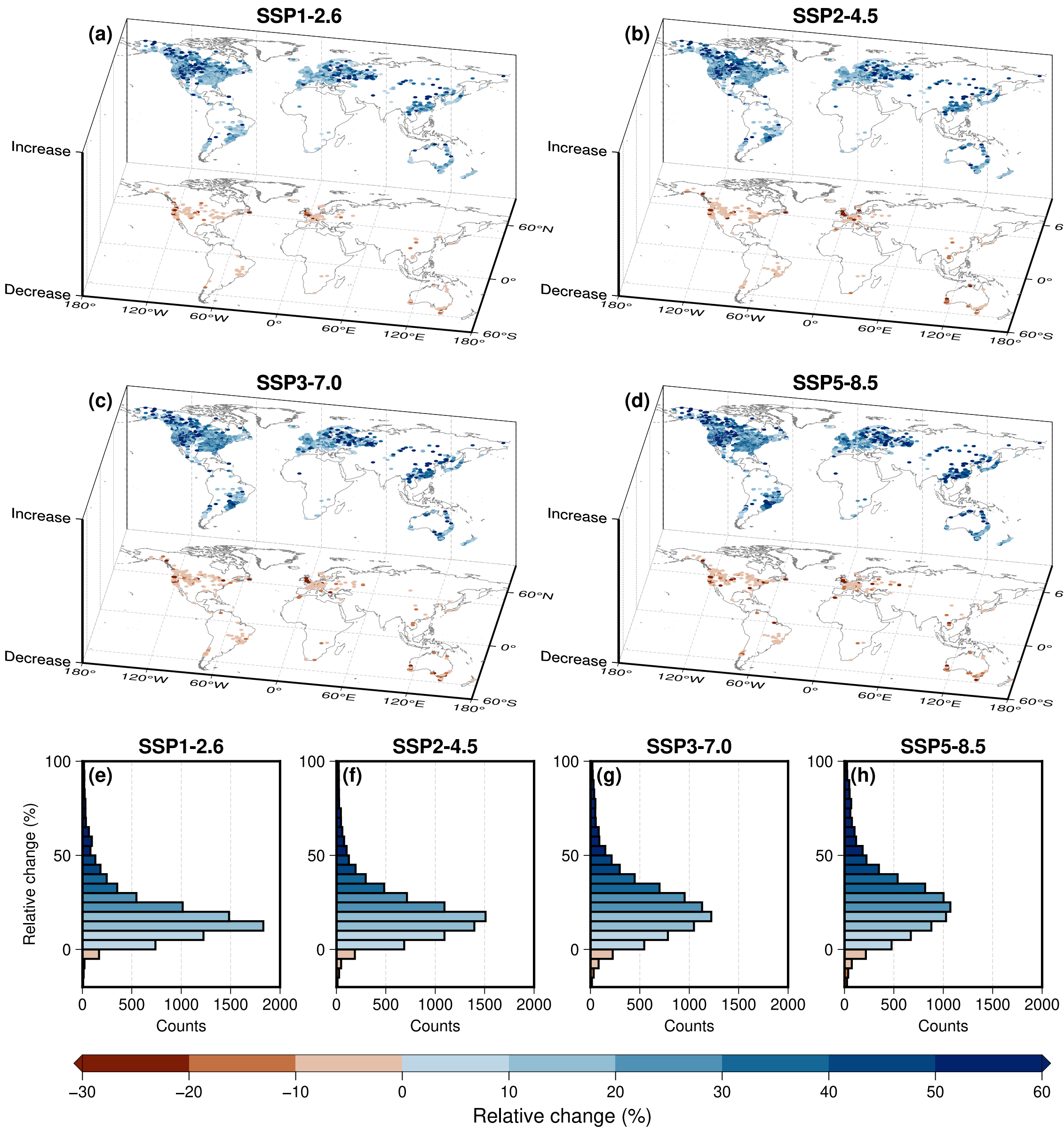

Figure 4. Multi-model ensemble mean relative change in future (2071–2100) flood peaks relative to historical (1985–2014) flood peaks under the 50-year return period for (a) SSP1-2.6, (b) SSP2-4.5, (c) SSP3-7.0, (d) SSP5-8.5, and (e–h) their respective histograms.

10%) exhibit a tendency to move in either direction. In the context of global warming, this phenomenon leads to fewer catchments with moderate changes. Instead, there is a noticeable shift toward the extremes, especially at the higher end of the spectrum. This pattern implies an escalating scenario of water inequality where some regions face disproportionately higher increases in flood risks compared to others. Simultaneously, there is a projection of increasing flood peaks and volumes in the majority of catchments. This trend necessitates the development of more robust and adaptive flood control strategies, as well as enhanced infrastructure planning to effectively mitigate the heightened risk of flooding and safeguard communities and ecosystems.

4.3. Joint Return Period Changes and Socioeconomic Implications

Meteorological disasters, owing to their varied and distinct characteristics, frequently result in significant socioeconomic losses, impacting communities and businesses on a large scale (Yin & Slater, 2023). Consequently, there is a pressing need to synthesize changes in bivariate flood risks to better understand and mitigate their

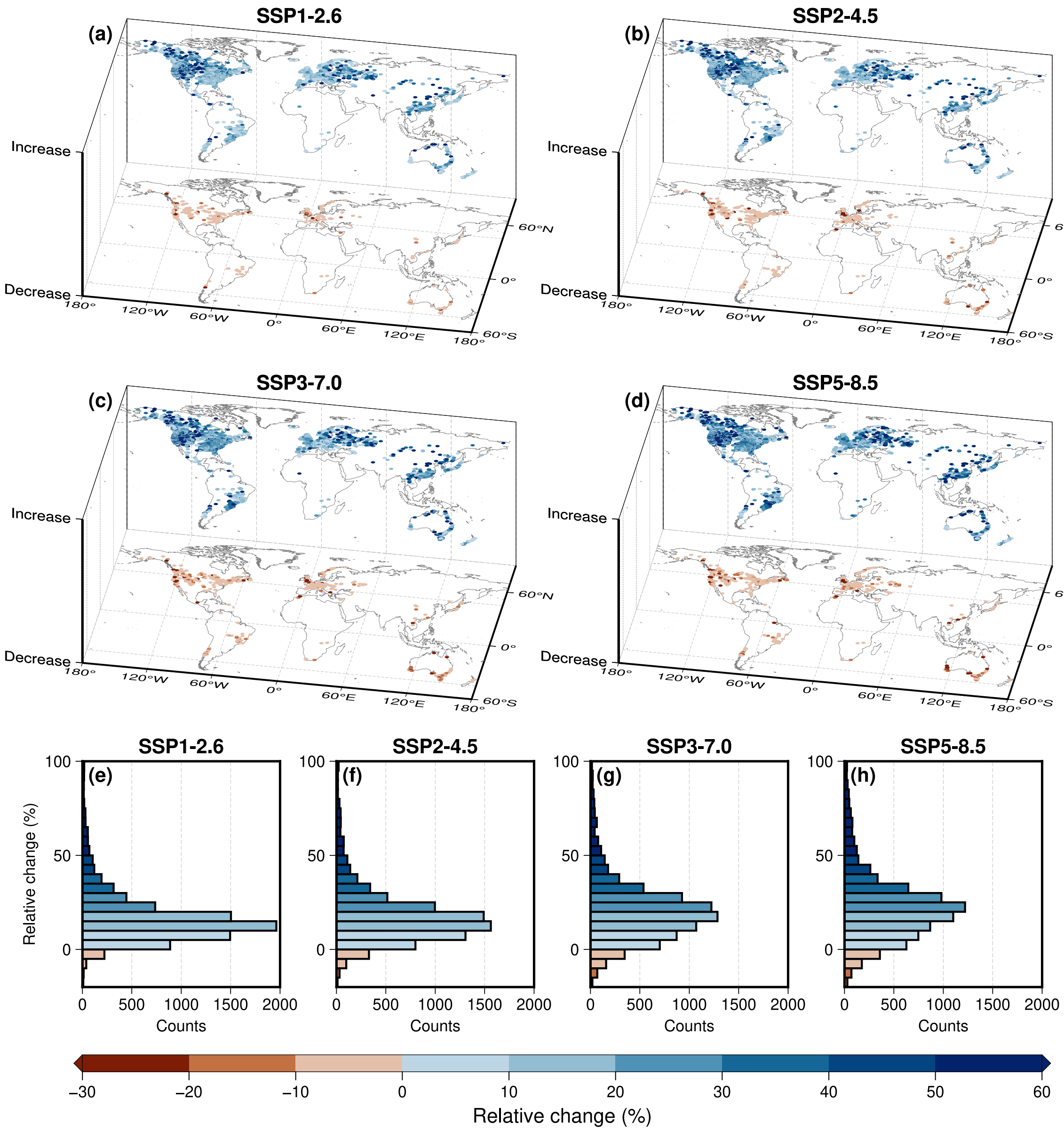

Figure 5. Multi-model ensemble mean relative change in future (2071–2100) flood volumes relative to historical (1985–2014) flood volumes under the 50-year return period for (a) SSP1-2.6, (b) SSP2-4.5, (c) SSP3-7.0, (d) SSP5-8.5, and (e–h) their respective histograms.

impacts. Figure 6 presents a detailed depiction of the changes in the JRP of a historical 50-year flood event from the historical period to future period under four different scenarios. Compared to the univariate analysis above, our study finds more catchments exhibiting an increased bivariate flood risk, as indicated by a decreased JRP. This heightened risk is attributed to the fact that in the bivariate context, either a flood peak or a flood volume can be considered a flood event if one of them meets the design criteria (i.e., the "OR" case). We observe that the number of catchments facing increased flood risk shows relatively minor variation across the 4 different scenarios, with 7,376 catchments under SSP1-2.6, 7,002 under SSP2-4.5, 7,152 under SSP3-7.0, and 7,173 under SSP5-8.5, out of a total of 8,583 catchments. However, a substantial trend is observed in the median JRP, which decreases as carbon emissions increase: the median JRP is 32.5-year for SSP1-2.6, reduces to 31.6-year for SSP2-4.5, further drops to 27.6-year for SSP3-7.0, and reaches its lowest at 25.7-year for SSP5-8.5. The projected decrease in median JRP suggests a nearly doubled flood frequency, underscoring the associated relationship between increased carbon emissions and escalating flood risk. Specifically, we observe that more than 95% of the catchments in China exhibit an increase in flood frequency under all four scenarios, which aligns with previous

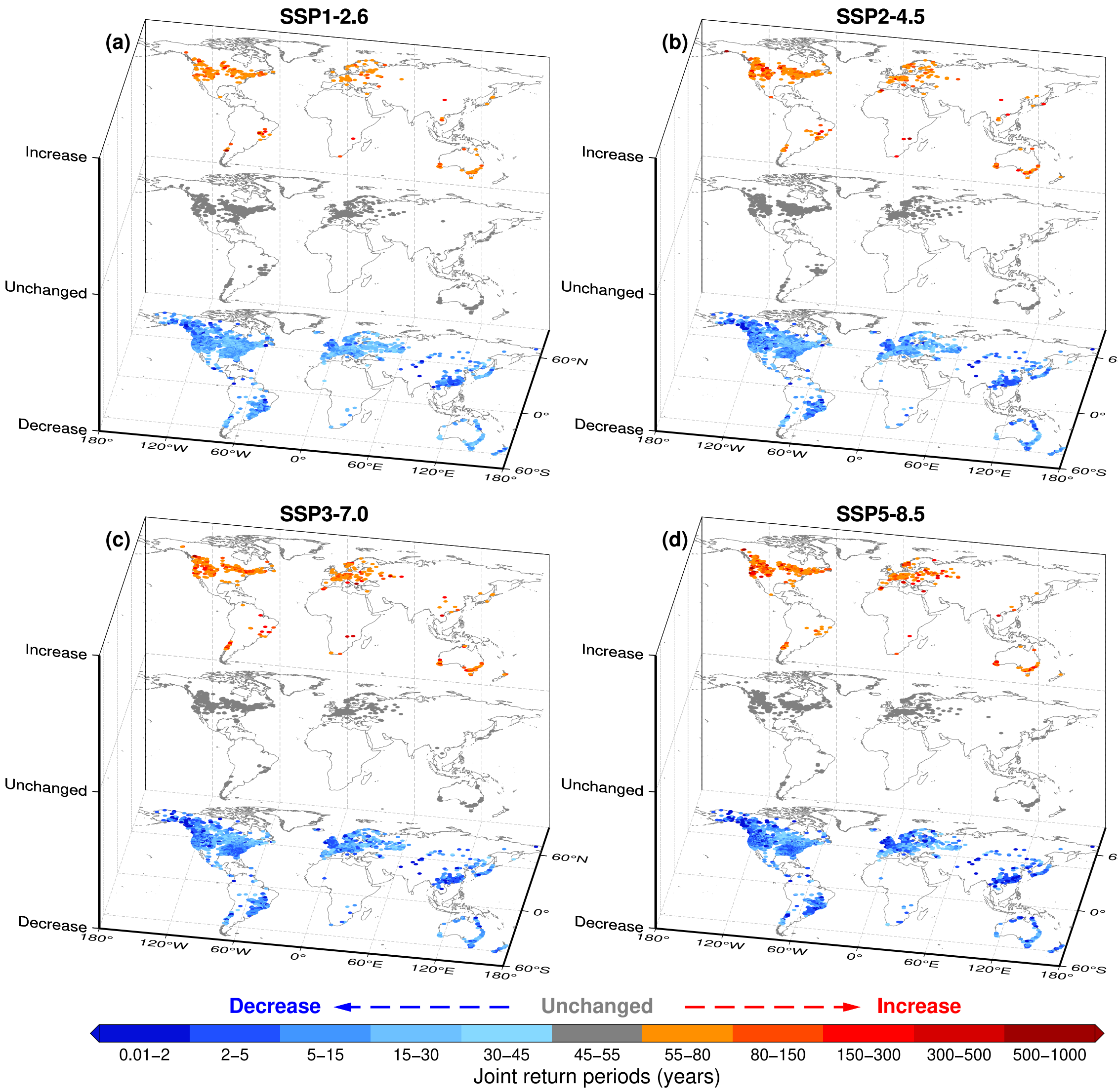

Figure 6. Multi-model ensemble mean future joint return period (JRP) of the historical 50-year flood event under (a) SSP1-2.6, (b) SSP2-4.5, (c) SSP3-7.0, and (d) SSP5-8.5. Each inset is divided into three layers, with the upper, middle, and lower layers representing the catchments where the JRP increases, stays the same, and decreases under the respective scenarios.

studies (Kang et al., 2023). Similarly, in the southeast region of the USA, comparable trends of consistently increasing flood frequencies have been observed (Kim & Villarini, 2024). Given that these two countries are among the world's largest economies, with large populations and rapidly growing economic sectors, it is urgent to quantify the socioeconomic implications of their increased flood risk. Understanding the socioeconomic implications is crucial in order to formulate effective strategies for mitigating the impact of floods in these economically vital areas.

Based on the future JRP analysis, we further segment the globe into five key subregions for a more granular investigation. These subregions are the USA, Europe, South America, East Asia, and Australia. Figures 7 and 8 present the projected population and GDP that are at risk of increased bivariate risk of flood peak and volume in the future period under SSP3-7.0. Despite a globally consistent trend of increasing flood risk, the socioeconomic implications show wide variation across different regions, primarily due to disparities in population density and the distribution of economic centers. For instance, in East Asia, which has a high concentration of economic activities and large population, the median GDP implication is estimated at 43 billion USD (Figure 7d), and the median population implication is around 2 million people (Figure 8d). As the world's 4th largest GDP, California

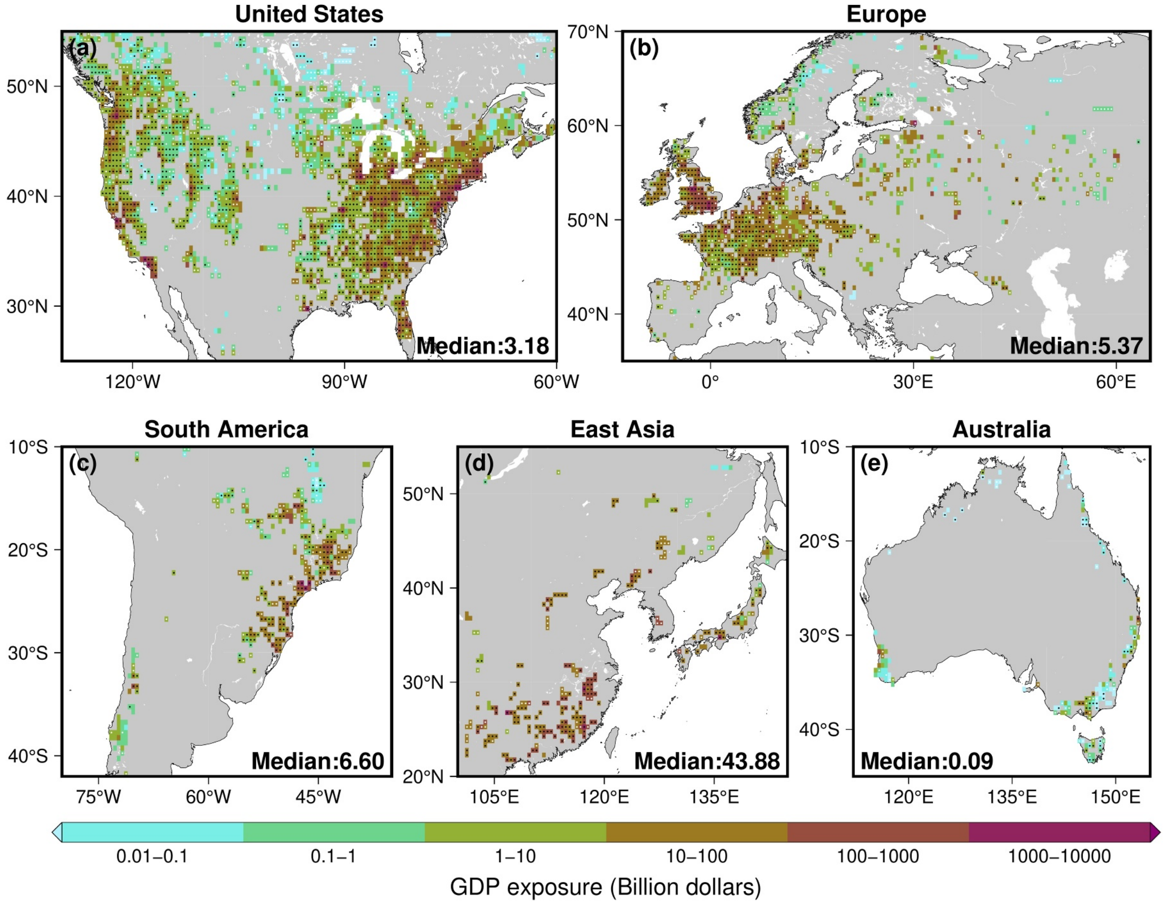

Figure 7. Implications of multi-model ensemble mean bivariate flood projections for GDP in the (a) USA, (b) Europe, (c) South America, (d) East Asia, and (e) Australia under SSP3-7.0 in the future period (2071–2100). Black (white) stippling denotes regions where the implications for GDP are statistically significant at the 99.9% (95%) confidence level.

exhibits a median population exposure of approximately 103,000 and a median GDP exposure of 9 billion USD. Conversely, in Australia, where population density and economic concentration are sparser, the implications are markedly different, with a median GDP implication of only 0.09 billion USD (Figure 7e) and a median population implication of about 1,000 people (Figure 8e). Even though the total exposure values for GDP and population are substantially higher in South America and East Asia, particularly China, compared to developed regions like the United States, Europe, and Australia, the per capita GDP exposure presents a contrasting trend, as shown in Figures S9–S12 in Supporting Information S1. The socioeconomic implications of carbon emissions exhibit substantial variations across different scenarios. In terms of GDP, the implications are highest under SSP5-8.5 (Figure S5 in Supporting Information S1) and lowest under SSP3-7.0 (Figure 7) across all regions. As for population implications, the highest levels are seen under SSP5-8.5 in the USA and Europe (Figures S8a and S8b in Supporting Information S1), while in East Asia, implications peak under the SSP3-7.0 scenario (Figure 8d).

To illustrate the robustness of the implications, we calculate the required minimum number of simulations l for each grid cell that consistently projects an increase in flood risk. In areas with high simulation densities like the US and Europe, a significance at the 99.9% (95%) level requires l to exceed 77(69) out of 120 simulations; while in regions with lower simulation densities, where only 20 GCMs are utilized, l needs to surpass 17 (14) to achieve the same level of significance. In our robustness analysis conducted on all grid cells, over 49% (76%) of the cells exhibit statistical significance at the 99.9% (95%) confidence level, regardless of the scenario considered. In regions such as the Andes, Eastern Europe, and southwestern Australia, there are notable uncertainties in the projections of socioeconomic implications. This variability is likely due to the influence of the westerly wind belt and the subtropical high-pressure belt, which lead to more divergent outcomes in climate model projections for these areas. Overall, our findings provide a comprehensive picture of the global socioeconomic implications of

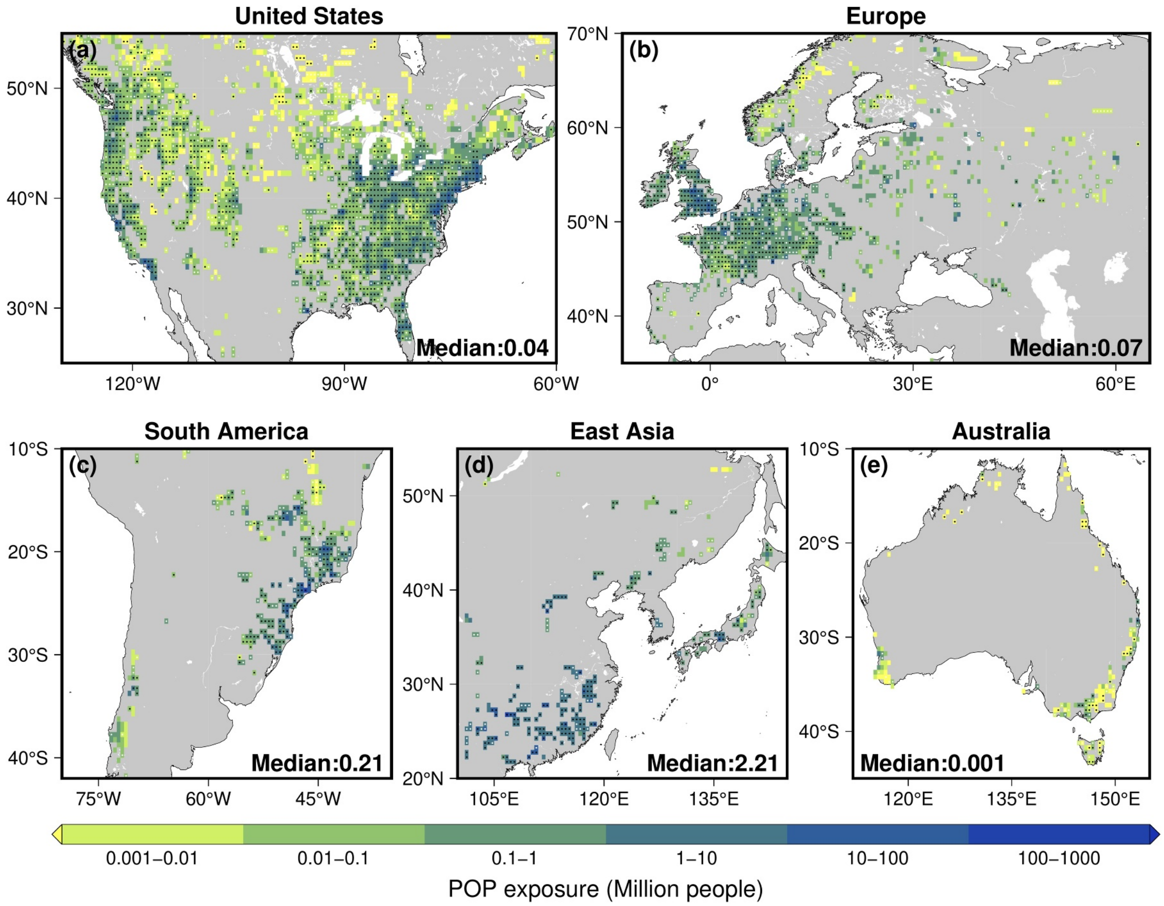

Figure 8. Implications of multi-model ensemble mean bivariate flood projections for population in the (a) USA, (b) Europe, (c) South America, (d) East Asia, and (e) Australia under SSP3-7.0 in the future period (2071–2100). Black (white) stippling denotes regions where the implications for population are statistically significant at the 99.9% (95%) confidence level.

flood risk under various emission scenarios. These results emphasize the critical need for equitable development across different emission pathways and the urgency to devise strategies aimed at averting significant demographic and economic losses.

4.4. Underlying Physical Mechanisms Behind Future Flood Evolution

By the end of the century, our planet is projected to be markedly warmer with more extreme weather events, influenced by increased greenhouse gas emissions and substantial alterations in global weather patterns (Shan et al., 2023). Through the examination of future changes in key meteorological variables, we aim to explore the physical mechanisms that contribute to the heightened global flood risk in the future. In Figure 9, we analyze the changes in the 99th percentile values, which are calculated by selecting the value at each grid point that exceeds 99% of all values annually, representing extreme meteorological conditions. The average values indicative of climate change are also shown under SSP3-7.0 in Figure S18 in Supporting Information S1. Although projections indicate only slight increases in future average daily precipitation, of less than 1 mm in most locations, and even small decreases in areas like the Mediterranean coast, Latin America, and southern Africa (Figure S18g in Supporting Information S1), there is a global rise in annual precipitation extremes, evidenced by a median increase of 3.66 mm (Figure 9g). This substantial rise in extreme precipitation events directly contributes to the escalating risk of flooding on a global scale, underscoring the changing patterns of weather extremes and their impact on flood risks. In addition, the phenomenon of decreasing relative humidity across extensive areas (Figure 9i), in the context of rising average and extreme high temperatures (Figures 9a–9c), hints at a non-linear relationship between evapotranspiration and global warming. This imbalance could lead to conditions more conducive to floods, as altered evapotranspiration patterns and warming temperatures may disrupt the natural

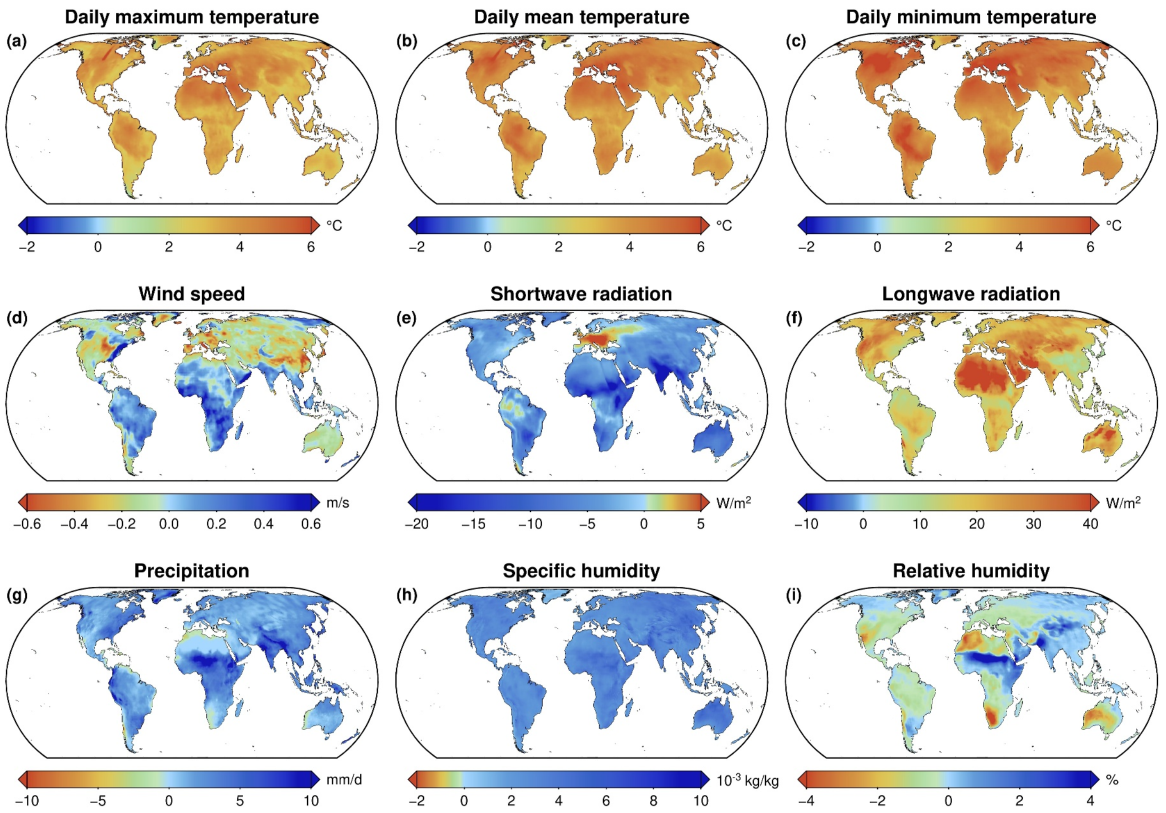

Figure 9. Multi-model ensemble mean changes in 99th percentile extreme values of various meteorological variables from the historical period (1985–2014) to the future period (2071–2100) under SSP3-7.0. (a–g) Changes of (a) daily maximum temperature, (b) daily mean temperature, (c) daily maximum temperature, (d) wind speed, (e) downwelling shortwave radiation, (f) downwelling longwave radiation, (g) precipitation, (h) specific humidity, and (i) relative humidity.

hydrological balance. The increase in mean downwelling surface shortwave radiation in Europe and the eastern US poses challenges for flood prevention (Figure S18e in Supporting Information S1). This is due to the mechanisms of ice and snow production and the dominant influence of radiation on streamflow in these regions, as detailed in Section 4.1. Coupled with the global greenhouse effect from increased emissions (Figures S18a–S18c, S18f, and S18h in Supporting Information S1), these hydrological changes are likely to significantly alter flood patterns in magnitude and frequency. Major adjustments will be required to existing flood management plans and control strategies in affected areas.

5. Discussion

By developing a physics-constrained DL framework, we capitalize on the memory structure inherent in these models, allowing for the inclusion of a broader range of relevant variables. Specifically, the RF model plays a crucial role in identifying the dominant meteorological factors for each catchment. These variables are then fed into the LSTM network, which uses the most pertinent data to simulate streamflow more accurately. Consequently, this hybrid modeling approach aims to markedly decrease the uncertainty in flood simulations and projections, especially in the relation to climate change, thereby enhancing the reliability of our future projections. Moreover, we employ the copula function to determine a correlation between flood peaks and 7-day flood volumes, enabling us to examine changes in the JRP of historical 50-year floods. Our findings indicate that under the SSPs, the JRP experiences a decrease in the majority of the catchments investigated. This decrease indicates that the median flood frequency is projected to be 1.5–2 times higher than current levels, highlighting a notable increase in flood occurrence across these regions. Furthermore, our analysis of the implications of increased flood risk for global GDP and populations highlights the potential for substantial economic and demographic losses in specific regions. Even under the most optimistic SSP1-2.6 scenario, trillions of USD in GDP and billions of people worldwide are still at risk of these enhanced flood threats. Additionally, for specific regions or countries, the socioeconomic implications resulting from changes under different scenarios are also substantial, indicating a direct correlation between policy decisions and the economic and demographic impacts of climate change.

Some limitations warrant consideration. Although the integration of lumped HMs with the physics-constrained DL framework improves model performance, the interpretability of the model still needs to be further improved. There are some studies based on novel explainable artificial intelligence (XAI) techniques that have yielded promising results in the field of climate science through the use of SHAP (SHapley Additive exPlanations, Mamalakis et al., 2023), LRP (Layer-wise Relevance Propagation, Mamalakis et al., 2022), and Gradient-based Attribution (Diffenbaugh & Barnes, 2023), etc. Efforts are still needed to make flood simulations more interpretable in future works. Streamflow simulation and attribution play critical roles in understanding how the terrestrial water cycle and water resources respond to global climate change. While GHMs are effective in projecting how flood regimes might change across extensive regions, their broad spatial coverage and inherent heterogeneity can impede detailed hydrological process descriptions (Gopalan et al., 2022). Future research can be devoted to refining global flood projections using GHMs and identifying the primary factors that drive streamflow changes. In addition, despite our efforts to gather the most credible and comprehensive in situ observation data available globally, it is important to note that certain critical regions which suffer from data sparseness, such as India and Africa, are expected to undergo rapid economic development by the end of this century. Recognizing this, we are committed to continuous efforts in further data collection and analysis, aiming to bridge these gaps and enhance the accuracy and scope of our hydrological assessments in these dynamically changing regions.

The global approach to carbon emissions mitigation remains divided (Daniel Tang, 2022; Y. Yang et al., 2024), yet the overarching goal of reducing losses from natural disasters stands as a shared vision for humanity. Our research clearly indicates the urgency of addressing global warming, leaving no time to waste in implementing effective control measures. In this context, the execution of the Sendai Framework for Disaster Reduction emerges as a crucial factor. It is important to recognize that different climate strategies may yield varying impacts both domestically and internationally for policymakers, highlighting the need to balance these differences carefully. In light of our findings, we advocate for stronger mitigation measures to reduce disaster risks, urging global governments to consider development equality in their strategic planning. This coordinated effort is essential for a sustainable and resilient future in the face of escalating climate challenges.

6. Conclusions

We utilize a RF model to decipher the physical mechanisms of runoff and then use a physics-constrained DL framework to project long-term streamflow under four scenarios (SSP1-2.6, SSP2-4.5, SSP3-7.0, and SSP5-8.5) across the globe. To understand the potential impact of future climate change, we analyze changes in the quantiles of future flood peaks and 7-day flood volumes for the future period (2071–2100) relative to the historical period (1985–2014), and employ copula functions to calculate the most likely realization of the JRP for the future period. Additionally, to assess the implications of these hydrological changes, we derive future socioeconomic implications based on projected changes in the bivariate flood peak and volume. The principal findings of this study are summarized as follows:

- Our integrated physics-constrained DL framework successfully enhances flood simulation from lumped hydrological models, improving the simulation accuracy in 40% of the catchments studied. The XAJ-LSTM and GR4J-LSTM models achieve the highest median KGE (0.76), reducing the uncertainty of future flood projections.
- Our study reveals that by the end of this century, the magnitudes of both flood peaks and volumes are expected to increase substantially in most catchments, with particularly notable escalations in regions such as the USA, Europe, and China. Within our bivariate flood framework, we observe that the JRP of historical 50-year flood events is projected to decrease to between 20 and 30 years in most catchments, indicating more frequent occurrence of flooding. The SSP5-8.5 scenario shows the most severe changes, with a median JRP decreasing to just 25.7-year, underlining the critical need for urgent emission reductions to limit these intensifying flood risks.
- Our research underscores the urgent need for global unity in addressing climate change, despite the current division in carbon emissions policies, to reduce losses arising from natural disasters—a goal shared by humanity. We highlight the vital importance of the Sendai Framework for Disaster Reduction and call for more

robust, equitable mitigation strategies to markedly lessen disaster risks, thereby securing a sustainable and resilient future amid intensifying climate challenges.

Conflict of Interest

The authors declare no conflicts of interest relevant to this study.

Data Availability Statement

The socioeconomic data set can be obtained from T. Jiang et al. (2024). The Climate Data Operator (CDO) is used for data processing (Schulzweida, 2023). The code in this study is provided by Kang (2024).

Acknowledgments

J.Y. acknowledges support from the Open Research Fund of Xinjiang Key Laboratory of Water Cycle and Utilization in Arid Zone, Xinjiang Institute of Ecology and Geography, Chinese Academy of Sciences (XJYS0907-2023-04), the National Natural Science Foundation of China (52441902, 52361145864, W2521014, and W2421111), and the Natural Science Foundation of Hubei Province (2024AFA055). L.S. acknowledges support from UKRI (MR/V022008/1) and NERC (NE/S015728/1).

References

Allan, R. P., Barlow, M., Byrne, M. P., Cherchi, A., Douville, H., Fowler, H. J., et al. (2020). Advances in understanding large-scale responses of the water cycle to climate change. *Annals of the New York Academy of Sciences*, *1472*(1), 49–75. https://doi.org/10.1111/nyas.14337

Bengtsson, L. (2010). The global atmospheric water cycle. *Environmental Research Letters*, *5*(2), 025202. https://doi.org/10.1088/1748-9326/5/2/025202

Berghuijs, W. R., Harrigan, S., Molnar, P., Slater, L. J., & Kirchner, J. W. (2019). The relative importance of different flood-generating mechanisms across Europe. *Water Resources Research*, *55*(6), 4582–4593. https://doi.org/10.1029/2019WR024841

Bergström, S., & Forsman, A. (1973). Development of a conceptual deterministic rainfall-runoff model. *Hydrology Research*, *4*(3), 147–170. https://doi.org/10.2166/nh.1973.0012

Botzen, W. J. W., Aerts, J. C. J. H., & Van Den Bergh, J. C. J. M. (2009). Dependence of flood risk perceptions on socioeconomic and objective risk factors. *Water Resources Research*, *45*(10), 2009WR007743. https://doi.org/10.1029/2009WR007743

Breiman, L. (2001). Random forests. *Machine Learning*, *45*(1), 5–32. https://doi.org/10.1023/A:1010933404324

Brunner, M. I. (2023). Floods and droughts: A multivariate perspective. *Hydrology and Earth System Sciences*, *27*(13), 2479–2497. https://doi.org/10.5194/hess-27-2479-2023

Brunner, M. I., Seibert, J., & Favre, A. (2016). Bivariate return periods and their importance for flood peak and volume estimation. *WIREs Water*, *3*(6), 819–833. https://doi.org/10.1002/wat2.1173

Chiew, F. H. S., Peel, M. C., Western, A. W., Singh, V. P., & Frevert, D. K. (2002). Application and testing of the simple rainfall-runoff model SIMHYD (pp. 335–367). Retrieved from https://api.semanticscholar.org/CorpusID:128731167

Dai, K., Shen, S., & Cheng, C. (2022). Evaluation and analysis of the projected population of China. *Scientific Reports*, *12*(1), 3644. https://doi.org/10.1038/s41598-022-07646-x

Daniel Tang, K. H. (2022). Climate change policies of the four largest global emitters of greenhouse gases: Their similarities, differences and way forward. *Journal of Energy Research and Reviews*, 19–35. https://doi.org/10.9734/jenrr/2022/v10i230251

Dellink, R., Chateau, J., Lanzi, E., & Magné, B. (2017). Long-term economic growth projections in the shared socioeconomic pathways. *Global Environmental Change*, *42*, 200–214. https://doi.org/10.1016/j.gloenvcha.2015.06.004

Diffenbaugh, N. S., & Barnes, E. A. (2023). Data-driven predictions of the time remaining until critical global warming thresholds are reached. *Proceedings of the National Academy of Sciences of the United States of America*, *120*(6), e2207183120. https://doi.org/10.1073/pnas.2207183120

Donat, M. G., Lowry, A. L., Alexander, L. V., O'Gorman, P. A., & Maher, N. (2016). More extreme precipitation in the world's dry and wet regions. *Nature Climate Change*, *6*(5), 508–513. https://doi.org/10.1038/nclimate2941

Fang, L., Yin, J., Wang, Y., Xu, J., Wang, Y., Wu, G., et al. (2024). Machine learning and copula-based analysis of past changes in global droughts and socioeconomic exposures. *Journal of Hydrology*, *628*, 130536. https://doi.org/10.1016/j.jhydrol.2023.130536

Frisbee, M. D., Phillips, F. M., Weissmann, G. S., Brooks, P. D., Wilson, J. L., Campbell, A. R., & Liu, F. (2012). Unraveling the mysteries of the large watershed black box: Implications for the streamflow response to climate and landscape perturbations. *Geophysical Research Letters*, *39*(1), 2011GL050416. https://doi.org/10.1029/2011GL050416

Gangrade, S., Kao, S., Naz, B. S., Rastogi, D., Ashfaq, M., Singh, N., & Preston, B. L. (2018). Sensitivity of probable maximum flood in a changing environment. *Water Resources Research*, *54*(6), 3913–3936. https://doi.org/10.1029/2017WR021987

Ganguli, P., & Merz, B. (2019). Extreme coastal water levels exacerbate fluvial flood hazards in northwestern Europe. *Scientific Reports*, *9*(1), 13165. https://doi.org/10.1038/s41598-019-49822-6

Gers, F. A., Schmidhuber, J., & Cummins, F. (2000). Learning to forget: Continual prediction with LSTM. *Neural Computation*, *12*(10), 2451–2471. https://doi.org/10.1162/089976600300015015

Gopalan, S. P., Champathong, A., Sukhapunnaphan, T., Nakamura, S., & Hanasaki, N. (2022). Potential impact of diversion canals and retention areas as climate change adaptation measures on flood risk reduction: A hydrological modelling case study from the Chao Phraya River Basin, Thailand. *Science of the Total Environment*, *841*, 156742. https://doi.org/10.1016/j.scitotenv.2022.156742

Gregorutti, B., Michel, B., & Saint-Pierre, P. (2017). Correlation and variable importance in random forests. *Statistics and Computing*, *27*(3), 659–678. https://doi.org/10.1007/s11222-016-9646-1

Gu, L., Chen, J., Yin, J., Sullivan, S. C., Wang, H.-M., Guo, S., et al. (2020). Projected increases in magnitude and socioeconomic exposure of global droughts in 1.5 and 2°C warmer climates. *Hydrology and Earth System Sciences*, *24*(1), 451–472. https://doi.org/10.5194/hess-24-451-2020

Han, J., Liu, Z., Woods, R., McVicar, T. R., Yang, D., Wang, T., et al. (2024). Streamflow seasonality in a snow-dwindling world. *Nature*, *629*(8014), 1075–1081. https://doi.org/10.1038/s41586-024-07299-y

Hirabayashi, Y., Tanoue, M., Sasaki, O., Zhou, X., & Yamazaki, D. (2021). Global exposure to flooding from the new CMIP6 climate model projections. *Scientific Reports*, *11*(1), 3740. https://doi.org/10.1038/s41598-021-83279-w

Hochreiter, S., & Schmidhuber, J. (1997). Long short-term memory. *Neural Computation*, *9*(8), 1735–1780.

Hoq, M. S., Raha, S. K., & Hossain, M. I. (2021). Livelihood vulnerability to flood hazard: Understanding from the flood-prone haor ecosystem of Bangladesh. *Environmental Management*, *67*(3), 532–552. https://doi.org/10.1007/s00267-021-01441-6

Hu, Y., Liang, Z., Huang, Y., Yao, Y., Wang, J., & Li, B. (2022). A nonstationary bivariate design flood estimation approach coupled with the most likely and expectation combination strategies. *Journal of Hydrology*, *605*, 127325. https://doi.org/10.1016/j.jhydrol.2021.127325

Jakeman, A. J., & Hornberger, G. M. (1993). How much complexity is warranted in a rainfall-runoff model? *Water Resources Research*, *29*(8), 2637–2649. https://doi.org/10.1029/93WR00877

Jiang, D., & Wang, K. (2019). The role of satellite-based remote sensing in improving simulated streamflow: A review. *Water*, *11*(8), 1615. https://doi.org/10.3390/w11081615

Jiang, T., Jing, C., Wang, Y., Zhai, J., Cao, L., Xu, X., et al. (2020). Possibility of implementing global sustainable development goals under the shared socioeconomic pathways. *Scientia Sinica Terrae*, *50*(10), 1445–1454. https://doi.org/10.1360/SSTe-2019-0158

Jiang, T., Su, B., Jing, C., Wang, Y., Huang, J., Guo, H., et al. (2024). National and provincial population and economy projection databases under Shared Socioeconomic Pathways (SSP1-5)_v2 (Version V4) [Dataset]. *Science Data Bank*. https://doi.org/10.57760/sciencedb.01683

Jiang, T., Zhao, J., Cao, L., Wang, Y., Su, B., Jing, C., et al. (2018). Projection of national and provincial economy under the shared socioeconomic pathways in China. *Climate Change Research*, *14*(1), 50–58. https://doi.org/10.12006/j.issn.1673-1719.2017.161

Kang, S. (2024). Code for "global flood projection and socioeconomic implications under a deep learning framework" [Software]. *Zenodo*. https://doi.org/10.5281/zenodo.11504215

Kang, S., Yin, J., Gu, L., Yang, Y., Liu, D., & Slater, L. (2023). Observation-constrained projection of flood risks and socioeconomic exposure in China. *Earth's Future*, *11*(7), e2022EF003308. https://doi.org/10.1029/2022EF003308

Kc, S., & Lutz, W. (2017). The human core of the shared socioeconomic pathways: Population scenarios by age, sex and level of education for all countries to 2100. *Global Environmental Change*, *42*, 181–192. https://doi.org/10.1016/j.gloenvcha.2014.06.004

Kim, H., & Villarini, G. (2024). Higher emissions scenarios lead to more extreme flooding in the United States. *Nature Communications*, *15*(1), 237. https://doi.org/10.1038/s41467-023-44415-4

Klingler, C., Schulz, K., & Herrnegger, M. (2021). LamaH-CE: LArge-SaMple DAta for hydrology and environmental sciences for central Europe. *Earth System Science Data*, *13*(9), 4529–4565. https://doi.org/10.5194/essd-13-4529-2021

Li, K., Huang, G., Wang, S., Razavi, S., & Zhang, X. (2022). Development of a joint probabilistic rainfall-runoff model for high-to-extreme flow projections under changing climatic conditions. *Water Resources Research*, *58*(6), e2021WR031557. https://doi.org/10.1029/2021WR031557

Liu, W., Yang, T., Sun, F., Wang, H., Feng, Y., & Du, M. (2021). Observation-constrained projection of global flood magnitudes with anthropogenic warming. *Water Resources Research*, *57*(3), e2020WR028830. https://doi.org/10.1029/2020WR028830

Mamalakis, A., Barnes, E. A., & Hurrell, J. W. (2023). Using explainable artificial intelligence to quantify "climate distinguishability" after stratospheric aerosol injection. *Geophysical Research Letters*, *50*(20), e2023GL106137. https://doi.org/10.1029/2023GL106137

Mamalakis, A., Ebert-Uphoff, I., & Barnes, E. A. (2022). Explainable artificial intelligence in meteorology and climate science: Model fine-tuning, calibrating trust and learning new science. In A. Holzinger, R. Goebel, R. Fong, T. Moon, K.-R. Müller, & W. Samek (Eds.), *XXAI - beyond explainable AI: International workshop, held in conjunction with ICML 2020, July 18, 2020, Vienna, Austria, revised and extended papers* (pp. 315–339). Springer International Publishing. https://doi.org/10.1007/978-3-031-04083-2_16

Mao, Y., Zhou, T., Leung, L. R., Tesfa, T. K., Li, H., Wang, K., et al. (2019). Flood inundation generation mechanisms and their changes in 1953–2004 in global major river basins. *Journal of Geophysical Research: Atmospheres*, *124*(22), 11672–11692. https://doi.org/10.1029/2019JD031381

Maurer, E. P., Kayser, G., Doyle, L., & Wood, A. W. (2018). Adjusting flood peak frequency changes to account for climate change impacts in the western United States. *Journal of Water Resources Planning and Management*, *144*(3), 05017025. https://doi.org/10.1061/(ASCE)WR.1943-5452.0000903

Mohanty, M. P., Vittal, H., Yadav, V., Ghosh, S., Rao, G. S., & Karmakar, S. (2020). A new bivariate risk classifier for flood management considering hazard and socio-economic dimensions. *Journal of Environmental Management*, *255*, 109733. https://doi.org/10.1016/j.jenvman.2019.109733

Muñoz-Sabater, J., Dutra, E., Agustí-Panareda, A., Albergel, C., Arduini, G., Balsamo, G., et al. (2021). ERA5-Land: A state-of-the-art global reanalysis dataset for land applications. *Earth System Science Data*, *13*(9), 4349–4383. https://doi.org/10.5194/essd-13-4349-2021

Nearing, G. S., Cohen, D., Dube, V., Gauch, M., Gilon, O., Harrigan, S., et al. (2024). Global prediction of extreme floods in ungauged watersheds. *Nature*, *627*(8004), 559–563. https://doi.org/10.1038/s41586-024-07145-1

Nearing, G. S., Kratzert, F., Sampson, A. K., Pelissier, C. S., Klotz, D., Frame, J. M., et al. (2021). What role does hydrological science play in the age of machine learning? *Water Resources Research*, *57*(3), e2020WR028091. https://doi.org/10.1029/2020WR028091

O'Neill, B. C., Carter, T. R., Ebi, K., Harrison, P. A., Kemp-Benedict, E., Kok, K., et al. (2020). Achievements and needs for the climate change scenario framework. *Nature Climate Change*, *10*(12), 1074–1084. https://doi.org/10.1038/s41558-020-00952-0

Ostad-Ali-Askari, K., Ghorbanizadeh Kharazi, H., Shayannejad, M., & Zareian, M. J. (2020). Effect of climate change on precipitation patterns in an arid region using GCM models: Case study of Isfahan-Borkhar plain. *Natural Hazards Review*, *21*(2), 04020006. https://doi.org/10.1061/(ASCE)NH.1527-6996.0000367

Park, T., Hashimoto, H., Wang, W., Thrasher, B., Michaelis, A. R., Lee, T., et al. (2023). What does global land climate look like at 2°C warming? *Earth's Future*, *11*(5), e2022EF003330. https://doi.org/10.1029/2022EF003330

Perrin, C., Michel, C., & Andréassian, V. (2003). Improvement of a parsimonious model for streamflow simulation. *Journal of Hydrology*, *279*(1–4), 275–289. https://doi.org/10.1016/S0022-1694(03)00225-7

Raju, K. S., & Kumar, D. N. (2020). Review of approaches for selection and ensembling of GCMs. *Journal of Water and Climate Change*, *11*(3), 577–599. https://doi.org/10.2166/wcc.2020.128

Sahu, M. K., Shwetha, H. R., & Dwarakish, G. S. (2023). State-of-the-art hydrological models and application of the HEC-HMS model: A review. *Modeling Earth Systems and Environment*, *9*(3), 3029–3051. https://doi.org/10.1007/s40808-023-01704-7

Samset, B. H., Stjern, C. W., Lund, M. T., Mohr, C. W., Sand, M., & Daloz, A. S. (2019). How daily temperature and precipitation distributions evolve with global surface temperature. *Earth's Future*, *7*(12), 1323–1336. https://doi.org/10.1029/2019EF001160

Samuels, P., Klijn, F., & Dijkman, J. (2006). An analysis of the current practice of policies on river flood risk management in different countries. *Irrigation and Drainage*, *55*(S1), S141–S150. https://doi.org/10.1002/ird.257

Schubert, S. D., Chang, Y., DeAngelis, A. M., Lim, Y.-K., Thomas, N. P., Koster, R. D., et al. (2024). Insights into the causes and predictability of the 2022/23 California flooding. *Journal of Climate*, *37*(13), 3613–3629. https://doi.org/10.1175/JCLI-D-23-0696.1

Schulzweida, U. (2023). CDO user guide (2.3.0) [Software]. *Zenodo*. https://doi.org/10.5281/zenodo.10020800

Shan, K., Lin, Y., Chu, P.-S., Yu, X., & Song, F. (2023). Seasonal advance of intense tropical cyclones in a warming climate. *Nature*, *623*(7985), 83–89. https://doi.org/10.1038/s41586-023-06544-0

Simmons, A. J., Untch, A., Jakob, C., Kallberg, P., & Unden, P. (1999). Stratospheric water vapour and tropical tropopause temperatures in ECMWF analyses and multi-year simulations. *Quarterly Journal of the Royal Meteorological Society*, *125*(553), 353–386. https://doi.org/10.1256/smsqj.55316

Smith, A., Bates, P. D., Wing, O., Sampson, C., Quinn, N., & Neal, J. (2019). New estimates of flood exposure in developing countries using high-resolution population data. *Nature Communications*, *10*(1), 1814. https://doi.org/10.1038/s41467-019-09282-y

Tang, R., Zhao, J., Liu, Y., Huang, X., Zhang, Y., Zhou, D., et al. (2022). Air quality and health co-benefits of China's carbon dioxide emissions peaking before 2030. *Nature Communications*, *13*(1), 1008. https://doi.org/10.1038/s41467-022-28672-3

Tellman, B., Sullivan, J. A., Kuhn, C., Kettner, A. J., Doyle, C. S., Brakenridge, G. R., et al. (2021). Satellite imaging reveals increased proportion of population exposed to floods. *Nature*, *596*(7870), 80–86. https://doi.org/10.1038/s41586-021-03695-w

Thrasher, B., Wang, W., Michaelis, A., Melton, F., Lee, T., & Nemani, R. (2022). NASA global daily downscaled projections, CMIP6. *Scientific Data*, *9*(1), 262. https://doi.org/10.1038/s41597-022-01393-4

Vousdoukas, M. I., Mentaschi, L., Voukouvalas, E., Bianchi, A., Dottori, F., & Feyen, L. (2018). Climatic and socioeconomic controls of future coastal flood risk in Europe. *Nature Climate Change*, *8*(9), 776–780. https://doi.org/10.1038/s41558-018-0260-4

Woldemeskel, F. M., Sharma, A., Sivakumar, B., & Mehrotra, R. (2014). A framework to quantify GCM uncertainties for use in impact assessment studies. *Journal of Hydrology*, *519*, 1453–1465. https://doi.org/10.1016/j.jhydrol.2014.09.025

Yang, S., Yang, D., Chen, J., Santisirisomboon, J., Lu, W., & Zhao, B. (2020). A physical process and machine learning combined hydrological model for daily streamflow simulations of large watersheds with limited observation data. *Journal of Hydrology*, *590*, 125206. https://doi.org/10.1016/j.jhydrol.2020.125206

Yang, Y., Yin, J., Kang, S., Slater, L. J., Gu, X., & Volchak, A. (2024). Quantifying the drivers of terrestrial drought and water stress impacts on carbon uptake in China. *Agricultural and Forest Meteorology*, *344*, 109817. https://doi.org/10.1016/j.agrformet.2023.109817

Yin, J., Gentine, P., Slater, L., Gu, L., Pokhrel, Y., Hanasaki, N., et al. (2023). Future socio-ecosystem productivity threatened by compound drought–heatwave events. *Nature Sustainability*, *6*(3), 259–272. https://doi.org/10.1038/s41893-022-01024-1

Yin, J., Guo, S., Yang, Y., Chen, J., Gu, L., Wang, J., et al. (2022). Projection of droughts and their socioeconomic exposures based on terrestrial water storage anomaly over China. *Science China Earth Sciences*, *65*(9), 1772–1787. https://doi.org/10.1007/s11430-021-9927-x

Yin, J., & Slater, L. (2023). Understanding heatwave-drought compound hazards and impacts on socio-ecosystems. *The Innovation Geoscience*, *1*(3), 100042. https://doi.org/10.59717/j.xinn-geo.2023.100042

Zhang, B., Wang, S., Qing, Y., Zhu, J., Wang, D., & Liu, J. (2022). A vine copula-based polynomial chaos framework for improving multi-model hydroclimatic projections at a multi-decadal convection-permitting scale. *Water Resources Research*, *58*(6), e2022WR031954. https://doi.org/10.1029/2022WR031954

Zhang, F., Biederman, J. A., Dannenberg, M. P., Yan, D., Reed, S. C., & Smith, W. K. (2021). Five decades of observed daily precipitation reveal longer and more variable drought events across much of the western United States. *Geophysical Research Letters*, *48*(7), e2020GL092293. https://doi.org/10.1029/2020GL092293

Zhang, S., Zhou, L., Zhang, L., Yang, Y., Wei, Z., Zhou, S., et al. (2022). Reconciling disagreement on global river flood changes in a warming climate. *Nature Climate Change*, *12*(12), 1160–1167. https://doi.org/10.1038/s41558-022-01539-7

Zhao, R. (1992). The Xinanjiang model applied in China. *Journal of Hydrology*, *135*(1), 371–381. https://doi.org/10.1016/0022-1694(92)90096-E

Zhou, Q., Luo, J., Su, J., & Ren, Y. (2021). Impacts of changing drainage indicators on urban flood volumes in historical urbanization in the case of northern China. *Urban Water Journal*, *18*(7), 487–498. https://doi.org/10.1080/1573062X.2021.1893366

Zhou, S., Williams, A. P., Lintner, B. R., Findell, K. L., Keenan, T. F., Zhang, Y., & Gentine, P. (2022). Diminishing seasonality of subtropical water availability in a warmer world dominated by soil moisture–atmosphere feedbacks. *Nature Communications*, *13*(1), 5756. https://doi.org/10.1038/s41467-022-33473-9

Zomer, R. J., Xu, J., & Trabucco, A. (2022). Version 3 of the global aridity index and potential evapotranspiration database. *Scientific Data*, *9*(1), 409. https://doi.org/10.1038/s41597-022-01493-1